Nanoscale

PAPER

View Article Online
View Journal

Cite this: DOI: 10.1039/d2nr07242d

Twist angle-dependent work functions in CVD-grown twisted bilayer graphene probed by Kelvin probe force microscopy†

Shangzhi Gu,‡[a,b] Wenyu Liu,‡[a] Shuo Mi,‡[a] Guoyu Xian,[b] Jiangfeng Guo,[a] Fei Pang,[a] Shanshan Chen, *[a] Haitao Yang, *[b] Hong-Jun Gao [b] and Zhihai Cheng *[a]

Tailoring the interlayer twist angle of bilayer graphene (BLG) significantly affects its electronic properties, including its superconductivity, topological transitions, ferromagnetic states, and correlated insulating states. These exotic electronic properties are sensitive to the work functions of BLG samples. In this study, the twist angle-dependent work functions of chemical vapour deposition-grown twisted bilayer graphene (tBLG) were investigated in detail using Kelvin probe force microscopy (KPFM) in combination with Raman spectroscopy. The thickness-dependent surface potentials of Bernal-stacked multilayer graphene were measured. It is found that with the increase in the number of layers, the work function decreases and tends to saturate. Bernal-stacked BLG and tBLG were determined *via* KPFM due to their twist angle-specific surface potentials. The detailed relationship between the twist angle and surface potential was determined *via in situ* KPFM and Raman spectral measurements. With the increase in the twist angle, the work function of tBLG will increase rapidly and then increase slowly when it is greater than 5°. The thermal stability of tBLG was investigated through a controlled annealing process. tBLG will become Bernal-stacked BLG after annealing at 350 °C. Our work provides the twist angle-dependent surface potentials of tBLG and provides the relevant conditions for the stability of the twist angle, which lays the foundation for further exploration of its twist angle-dependent electronic properties.

Received 27th December 2022,
Accepted 17th February 2023

DOI: 10.1039/d2nr07242d

rsc.li/nanoscale

Introduction

Graphene, a two-dimensional (2D) material, has attracted considerable attention owing to its unique electronic, optical, and mechanical properties. The electronic properties of graphene depend significantly on the stacking orientation of the layers. For instance, in the case of twisted bilayer graphene (tBLG), the electronic band structure is significantly changed. tBLG has been proven to exhibit different physical properties from Bernal-stacked bilayer graphene (BLG), *e.g.* the Moiré patterns resulting from the twisted stacking layers at a small angle. In particular, at a small magic twist angle, BLG transforms from a weakly correlated Fermi liquid into a strongly correlated 2D electron system with exotic properties such as unconventional superconductivity,[1–3] topological transitions,[4] magnetic transport characteristics,[5] and Mott-correlated electronic states.[6,7]

Among the several methods for preparing 2D materials, chemical vapour deposition (CVD) is the most popular one. CVD-grown graphene films with specific thicknesses and high crystalline quality have been successfully prepared.[8,9] The growth of tBLG *via* CVD is important for the investigation of its angle-dependent physical properties and potential applications.[10–15] In addition, it is critical to directly characterise the angle-dependent structural characteristics of tBLG. Recently, transmission electron microscopy,[16,17] micro-Raman spectroscopy,[18,19] and various scanning probe microscopy (SPM) techniques[20–26] have been widely used to study the Moiré patterns of tBLG samples constructed using artificial stacking methods. For CVD-grown twisted graphene layers, the angle-dependent structural and vibrational characteristics of tBLG have been revealed by Raman spectroscopy.[27–31]

From a spatial-resolution perspective, SPM-based approaches are promising for the characterisation of their electronic properties. Non-monotonic angle-dependent vertical electrical conductivity across the interface of tBLG was discovered using conductive atomic force microscopy (C-AFM).[32] The electronic properties of tBLG films are sensitive to their local work functions and surface potentials. As a starting point,

[a]*Beijing Key Laboratory of Optoelectronic Functional Materials & Micro-nano Devices, Department of Physics, Renmin University of China, Beijing 100872, China. E-mail: schen@ruc.edu.cn, zhihaicheng@ruc.edu.cn*
[b]*Beijing National Laboratory for Condensed Matter Physics, Institute of Physics, Chinese Academy of Sciences, P.O. Box 603, Beijing 100190, China. E-mail: htyang@iphy.ac.cn*

†Electronic supplementary information (ESI) available. See DOI: https://doi.org/10.1039/d2nr07242d

‡These authors contributed equally to this work.

there is an urgent need to identify rotation-related bilayer domains with microscale resolution in CVD-grown tBLG films and quantitatively measure their angle-dependent work functions. For measuring the surface potentials and work functions, Kelvin probe force microscopy (KPFM) has proven to be an excellent technique with outstanding resolution and sensitivity.[33,34] Relevant work has been done using KPFM technology to study the relationship between the work function of stripped graphene and the number of layers.[35–38] In 2018, Robinson *et al.* measured the surface potential between layers with different twist angles or layer thicknesses in graphene obtained by chemical vapor deposition and combined it with Raman technology to resolve different twist angles.[39] However, at present, there is no direct use of KPFM technology to directly use pictures to distinguish different graphite torsion angles with different work functions. In addition, it is rarely useful to study the thermal stability of tBLG using KPFM technology.

In this study, we performed a comprehensive KPFM investigation of the surface potentials of CVD-grown multilayer graphene films with different thicknesses and twist angles, in combination with Raman spectroscopy. First, the thickness-dependent surface potential of the Bernal-stacked multilayer graphene film was measured and directly resolved by KPFM. Thus, we could directly distinguish BLG from tBLG according to their different surface potentials. The twist angle-dependent surface potentials of tBLG were investigated in detail through *in situ* KPFM. Additionally, the thermal stability of tBLG was investigated using a controlled sequential annealing process.

Results and discussion

The multilayer graphene films were synthesised using a modified low-pressure CVD system.[15] A schematic of the experimental CVD setup is shown in Fig. 1(a). By controlling the growth conditions, high-quality graphene grains with sizes of several hundred microns were obtained. For multilayer graphene, the second layer is formed beneath the first layer owing to the reaction of the catalysed copper surfaces. The growth mode of the multilayer graphene films is illustrated in Fig. 1(a). After the growth, large-area graphene films were transferred onto an SiO_2/Si substrate using the polymethyl methacrylate (PMMA) wet transfer process.[40,41]

Fig. 1(b) shows an optical image of a typical multilayer graphene film on an SiO_2/Si substrate. The single-layer (1L), bilayer (2L), and trilayer (3L) graphene regions were clearly resolved according to their specific optical contrast. The top graphene layer was continuous and covered the entire SiO_2/Si substrate. For the partial 2L region, the second layer was under the top layer, and for the partial 3L region, the third layer was under the bilayer and directly on the bottom substrate. Fig. 1(c) shows a scanning electron microscopy (SEM) image of the multilayer graphene films in Fig. 1(b). It provides the layer-number contrast and distributions of the 1L, 2L, and 3L regions. Even with differential interference contrast optical

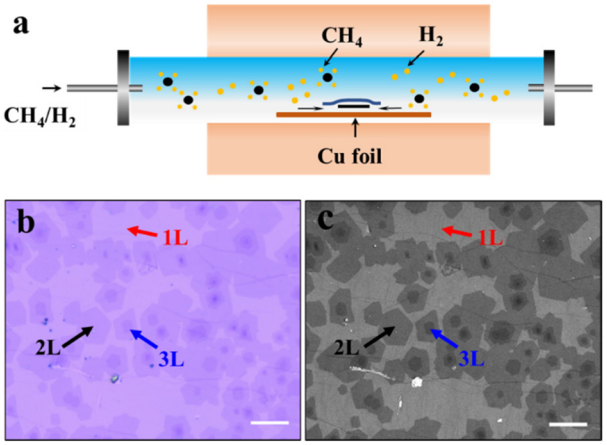

Fig. 1 Optical and SEM characterisation of the CVD-grown multilayer graphene films. (a) Schematic of the CVD growth process of multilayer graphene on copper foil. The new graphene layer (black) nucleates below the single layer (blue). (b) Optical image of a multilayer CVD graphene film transferred onto an SiO_2/Si substrate. (c) SEM image of multilayer graphene shown in (b). The single-layer (1L), bilayer (2L), and trilayer (3L) graphene regions are indicated by arrows and determined by their relative contrast. No interior crystalline or twisted domains of the multilayer graphene films are observed in (b) or (c). The scale bar represents 70 μm in (b) and (c).

and SEM images, the interior crystalline and twisted domains of the multilayer graphene films were not discernible. Our work provides the twist angle-dependent surface potentials of tBLG and lays the foundation for further exploration of their twist angle-dependent electronic properties.

Many electrical SPM techniques, such as scanning microwave impedance microscopy, electrostatic force microscopy (EFM), C-AFM, and KPFM, have been used to investigate the local electrical properties of 2D materials.[32,42–45] KPFM is an atomic force microscopy (AFM) technique for spatially mapping and studying the surface topography and local work function variations simultaneously under ambient conditions.[37,40,46] The spatial resolution in the KPFM mode was ~700 nm and the voltage resolution was ~1.8 mV. Electrical characterisation of CVD-grown multilayer graphene films was performed using KPFM to measure their local work functions. The work function is an intrinsic band property of the material that quantifies the minimum energy required to bring an electron from the Fermi level (E_F) to the vacuum level (E_V).

As shown in Fig. 2(a), a conductive AFM tip was electrically biased (V_{dc} + V_{ac}) against a ground sample. The bias-dependent electrostatic force between the tip and the sample was measured and minimised by adjusting V_{dc} *via* KPFM feedback. The measured V_{dc} voltage of the bias tip, corresponding to the contact-potential difference (V_{CPD}), determined the work-function difference between the AFM tip and the targeted region of the graphene film (Fig. S4†). V_{CPD} was related to the work functions of the tip (W_{tip}) and the sample as follows: $-eV_{CPD} = W_{sample} - W_{tip}$, where e represents the elementary charge.

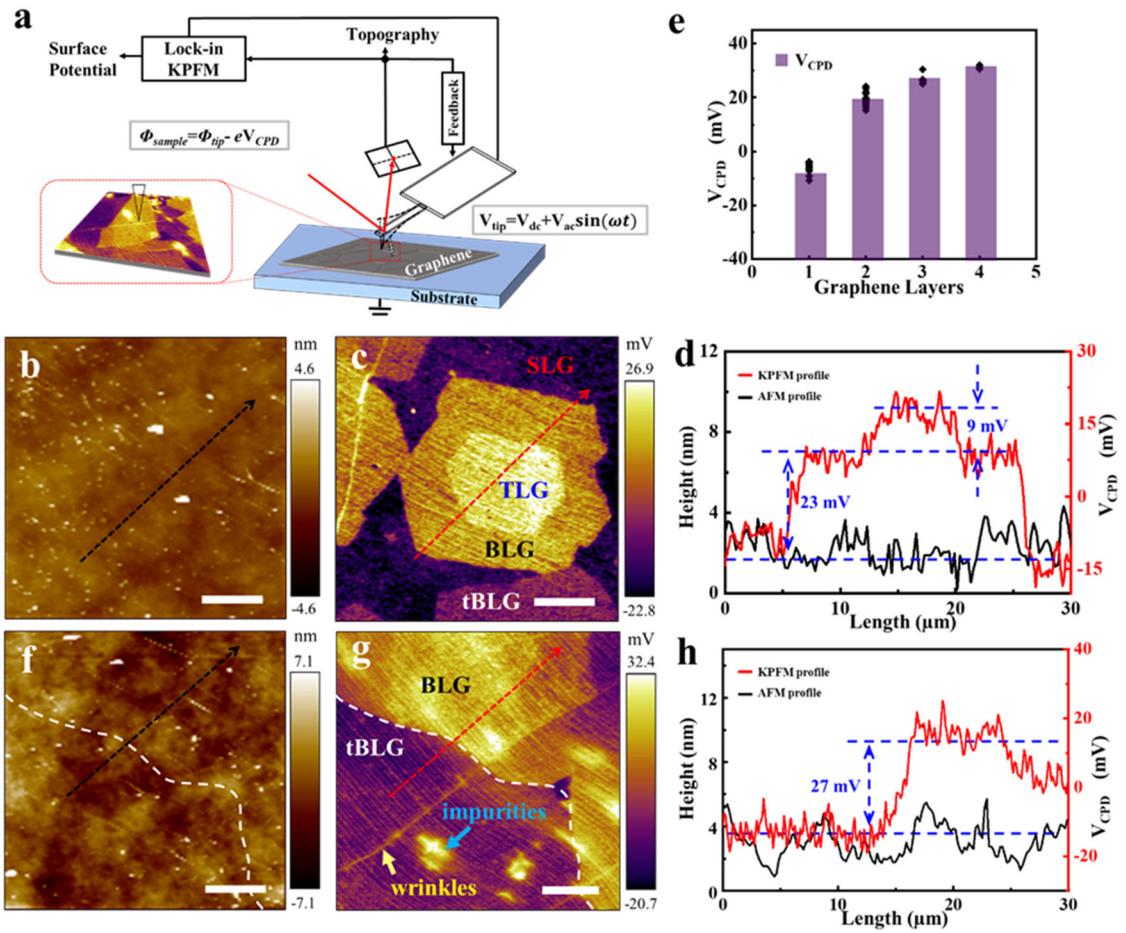

Fig. 2 KPFM characterisation of CVD-grown multilayer graphene transferred onto the SiO_2/Si substrate. (a) Schematic of the KPFM setup. (b) Topographical image of a conventional multilayer graphene region. (c) Surface potential image corresponding to (b) obtained *via* KPFM. (d) Cross-sectional profiles of the topography in (a) and surface potential in (c). (e) Histogram of the average surface potentials of Bernal-stacked monolayer, bilayer, trilayer and tetralayer graphene. (f) Topographical image of a BLG region. (g) Surface potential image corresponding to (f). Two specific areas with different surface potentials are clearly observed in (g), which correspond to AB-BLG and tBLG, respectively. The interior grain boundary of the BLG region is highlighted by white dashed lines in (f) and (g). The yellow and blue arrows indicate the typical graphene wrinkles and surface contaminations. (h) Cross-sectional profiles of the topography in (f) and surface potential in (g). The scale bar represents 6 μm in all the AFM images.

Through the KPFM measurements, we obtained a V_{CPD} value. During the experiment, we assumed that the surface potential of the AFM tip remained unchanged. The value of V_{CPD} reflected the change in the surface potential of the sample and corresponded to the change in the vacuum energy level. If the work function of the tip was known, the work function (or surface potential) of each point on the sample surface could be obtained.

Fig. 2(b) shows the AFM topography of a typical multilayer graphene region. The layer–number relationship (*i.e.* 1L, 2L, and 3L) was determined *via* optical microscopy. Raman features confirmed that the two- and three-layer regions had AB and ABA stacked configurations, respectively. The AB-BLG and ABA-TLG regions were determined and named BLG and TLG, respectively. The thicknesses of the graphene layers were not distinguishable in the topographic image, owing to the underlying growth mode and surface roughness of the SiO_2/Si substrate. The SLG, BLG, and TLG regions were clearly distinguished by their specific surface potentials, as shown in Fig. 2(c). The corresponding line profiles of the topography and surface potential shown in Fig. 2(b) and (c), respectively, are presented in Fig. 2(d). The V_{CPD} of TLG (BLG) was ~9 mV (~23 mV) higher than that of BLG (SLG). This indicated that the surface potential of TLG (BLG) was higher than that of BLG (SLG). It is found that the work function will decrease with the increase in the number of layers, which is consistent with the theoretical calculations of Ziegler.[38] Fig. 2(e) shows the thickness-dependent surface potentials of Bernal-stacked monolayer (SLG), bilayer (BLG), trilayer (TLG), and tetralayer graphene. The surface potentials increased monotonically with an increase in the thickness of the graphene layers, indicating that the work function decreased with the increasing graphene layer thickness. In the wet transfer process, the sample may introduce p-doping, so the work function decreases with the increase in layer thickness, which is in contrast to the trend of graphene in the previous article.[39] Moreover, due to the influ-

ence of interlayer screening,[38] when the number of layers is more than two, the value of work function tends to be saturated gradually.

When a twist angle is introduced into BLG, the entire band structure and thus the Fermi level may change.[39,47] Therefore, work functions can serve as fingerprints for characterising tBLG domains with different twist angles. Fig. 2(f) and (g) show the simultaneously obtained AFM and KPFM images of one selected BLG region from the optical image. The optical image shows that these two regions are both double-layer structures, but there are different contrasts in the KPFM signal, which may be due to the different twist angles. The interior domain boundary of this BLG is indicated by dashed lines. Typical wrinkles are clearly observed in Fig. 2(g), which may follow the polishing striations of the copper substrate and may have been formed during the CVD-growth process. Cluster-like surface contaminations resulting from the transfer process are also observed as shown in Fig. 2(g). The shape of the lustre-like surface contaminations is generally irregular and can be well distinguished from the sample; thus, the sample area could be accurately determined. The cross-sectional topography and surface potential profiles are shown in Fig. 2(h). There was a surface potential difference of ~27 mV between the two bilayer areas, owing to their different twist angles. This type of graphene, which differs from BLG, is called tBLG. Therefore, using optical microscopy and KPFM, we could directly distinguish Bernal-stacked multilayer graphene films from tBLG according to their different surface potentials.

Raman spectral measurements were performed on these twisted multilayer graphene films, as shown in Fig. 3. Fig. 3(a) presents the Raman spectra of SLG, BLG, tBLG ($\theta < 3°$), and tBLG ($\theta \approx 30°$). The Raman modes for the G- and 2D-bands of SLG were located at approximately 1576 and 2702 cm^{-1}, respectively. For SLG, the intensity of the G peak was significantly lower than that of the 2D peak. For Bernal-stacked BLG, the intensity of the G peak was higher than that of the 2D peak.

The 2D-to-G intensity ratio (I_{2D}/I_G) was used to determine the twist angles of BLG.[29–31] For the CVD-grown graphene samples used in this study, the twist angles of tBLG were grouped into four regimes: $\theta < 3°$, $3° < \theta < 8°$, $12° < \theta < 15°$, and $\theta \approx 30°$. The 2D full width at half maximum (FWHM) of tBLG ($\theta < 3°$) was larger and smaller than those of SLG and BLG, respectively. The origin of the larger 2D FWHM in this small-twist angle regime was complex because of the local Bernal AB/BA stacking configurations resulting from interfacial relaxation.[30,48] The I_{2D}/I_G ratio (2D FWHM) of tBLG ($\theta \approx 30°$) was slightly larger (smaller) than that of SLG, which was attributed to the weak interlayer coupling. The emergence of the D-like peak (~1348 cm^{-1}) and the R peak (~1369 cm^{-1}) was attributed to the intrinsic quasicrystal states.[49–51] The R'-band at ~1625 cm^{-1} was unique to tBLG with $3° < \theta < 8°$, as shown in Fig. 3(b). For tBLG ($12° < \theta < 15°$), the characteristic R-band appeared at ~1476 cm^{-1} in the Raman spectra, as shown in Fig. 3(c). For this twist-angle regime, a plot of the R-peak position *versus* the twist angle is shown in Fig. S1,† which exhibits a trend similar to that in ref. 52. The high intensity of the G-band in this regime was due to enhanced Van Hove singularities. Fig. 3(d) shows a plot of the 2D peak FWHM *versus* the twist angle in the four regimes for tBLG. To illustrate the trend of the 2D FWHM as a function of the twist angle, we plotted the shaded circles and red dashed lines of the experimental data collection, as shown in Fig. 3(d). Clearly, tBLG preferred four specific twist-angle regimes in the CVD-grown multilayer graphene films. Compared with previous studies,[53,54] a sharp increase in the 2D FWHM at the twist angles of 7°–9° was not observed because of the absence of tBLG in this regime.

Fig. 3(e) and (f) show the corresponding optical image and the Raman 2D FWHM map of the CVD-grown multilayer graphene films. It can be clearly seen that the contrast of TLG is significantly higher than that of BLG, which is consistent with the results we obtained using KPFM. The tBLG regions are clearly observed in Fig. 3(f), which mainly exist as single BLG flakes or as a part of BLG flakes with interior tBLG and BLG domains. A statistical analysis indicated that the single flakes or domains of tBLG preferred a twist angle of $\theta \approx 30°$ in our CVD-grown graphene films. TLG flakes with twisted trilayer graphene (tTLG) and ABA-stacked domains were also obtained, as shown in Fig. 3(f). The formation mechanism of these twisted graphene layers is unclear and may be related to the underlying growth mode of the multilayer graphene.

In situ Raman and KPFM measurements were further performed to correlate the various surface potentials and twist angles of tBLG, as shown in Fig. 4. Fig. 4(a) presents the Raman 2D peak FWHM mapping of Bernal-stacked multilayer graphene and a single tBLG region with a twist angle of $27° < \theta < 30°$. The corresponding surface potential image shows a clear contrast between the single tBLG and BLG domains (Fig. 4(b)). The surface potential difference between the tBLG ($27° < \theta < 30°$) and BLG domains was ~25 mV, as shown in the histogram in Fig. 4(c). Fig. 4(d) and (e) show the corresponding Raman 2D peak FWHM and KPFM surface potential mapping of one BLG region with interior tBLG ($3° < \theta < 8°$) and BLG domains. The surface potential difference between the interior tBLG ($3° < \theta < 8°$) and BLG domains was determined to be ~13 mV, as shown in Fig. 4(f). Fig. 4(g and h) show the surface potential images of different BLG areas. It can be clearly seen that there are differences in tBLG and BLG between the same layers. The potential changes in these two angular ranges were consistent with those reported by Robinson *et al.*[39] They reported a difference of 32 meV between BLG with small and large twist angles, which is consistent with our KPFM results. In addition, they reported that at a twist angle of 15°, the V_{CPD} was approximately 5 meV smaller than its value at larger angles, which agrees well with Fig. 4(i) of the present work. In this aspect, our work and the previous article support each other well. On the other hand, our results also show that the introduction of p-doping into graphene does not affect the work function of the bilayer with respect to the angle. Additionally, the wrinkles of the graphene layer were clearly observed in both the Raman and KPFM mappings, as indi-

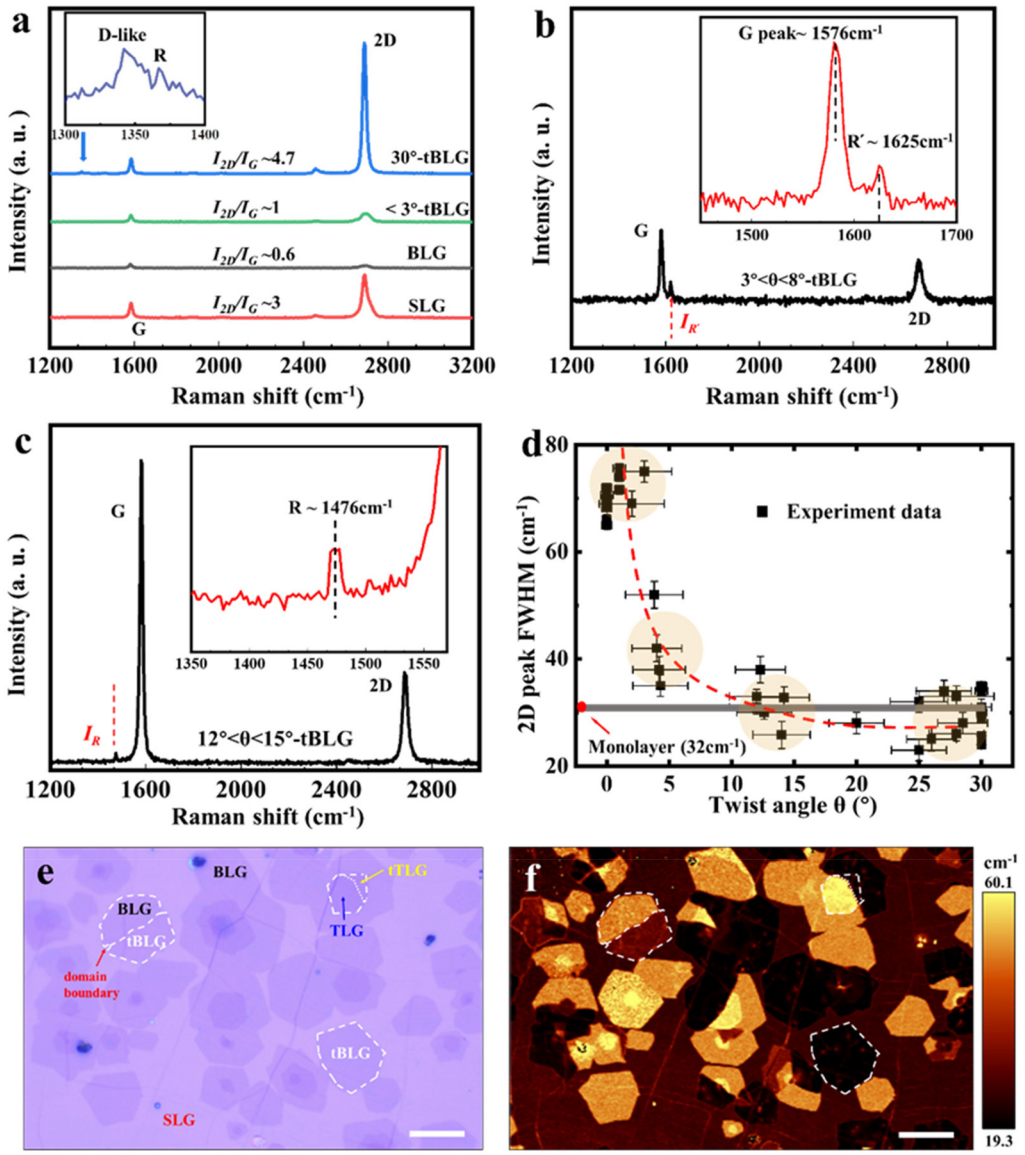

Fig. 3 Raman characterisation of CVD-grown BLG. (a) Raman spectra of SLG and tBLG with different twist angles. Only wavenumber ranges near the G and 2D peaks are shown. The Raman spectrum of each curve has been vertically shifted for clarity. The red, black, green, and blue curves represent the Raman spectra of SLG, BLG, tBLG (twist angle of $\theta < 3°$), and tBLG ($\theta \approx 30°$), respectively. The inset shows a magnified view of the D-like peak and R peak for tBLG ($\theta \approx 30°$). (b) Raman spectra of tBLG ($3° < \theta < 8°$). Inset: the Raman peak of the R′-band at ~1625 cm^{-1}. (c) Raman spectra of tBLG ($12° < \theta < 15°$). Inset: the Raman peak of the R-band at ~1476 cm^{-1}. The θ-dependent Raman spectral features of the R- and R′-bands resulted from the static interlayer potential-mediated inter- and intra-valley double-resonance Raman scattering processes. (d) Plot of the 2D peak FWHM *versus* the twist angle (θ) for tBLG. The shaded circles show clusters of the experimental data, and the red dashed line is for visual guidance. (e) Optical image of CVD-grown multilayer graphene on the SiO_2/Si substrate. (f) Raman 2D FWHM mapping for the area shown in (e). The scale bar represents 30 μm in (e) and (f). tBLG can exist as a single BLG flake or a part of a BLG flake with interior tBLG and BLG domains.

cated by the yellow arrow. The domain boundary between tBLG and BLG (marked by white arrows) is shown as a sharp change in contrast, and there were no wrinkles at the domain boundary, as observed in both the Raman and KPFM mappings. However, no enhancement or reduction in the signal contrast due to domain boundaries was observed at the junction of the domain regions. It can be concluded that the tBLG and BLG domains were atomically and smoothly merged without mechanical strain.[55–57]

Additional optical, SEM, Raman, and KPFM measurement results for the tBLG films are presented in Fig. 2(g) and (h) and Fig. S2–S4.† Fig. 4(i) shows a plot of the surface potential (SP) difference $\Delta\Phi$ ($\Delta\Phi = SP_{BLG} - SP_{tBLG}$) between tBLG and BLG *versus* the twist angle (θ) of tBLG. Generally, the $\Delta\Phi$ of tBLG increased monotonically with an increase in the twist angle (θ). For tBLG ($\theta < 3°$), $\Delta\Phi$ was small. With an increase in θ, it rapidly increased to approximately 15–20 mV ($\theta \approx 5°$) and then slowly increased to ~25 mV ($\theta \approx 30°$). As θ increased, the

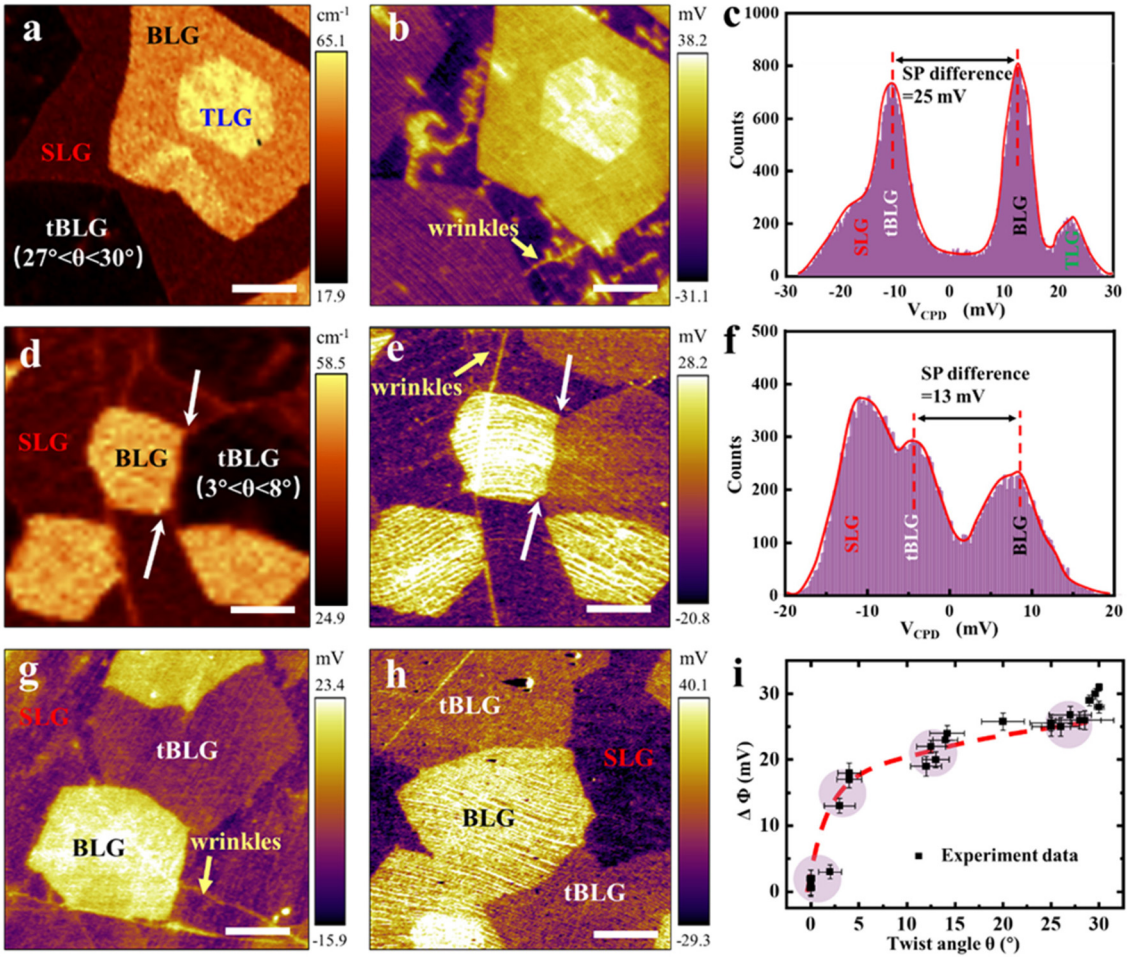

Fig. 4 Raman and KPFM characterisations of CVD-grown multilayer graphene. (a) Raman 2D peak FWHM mapping of a conventional multilayer graphene region with a single tBLG flake. (b) Surface potential image corresponding to (a). (c) Histogram of the surface potentials in (b), indicating a potential difference of ~25 mV between tBLG and BLG. (d) Raman 2D peak FWHM mapping of a BLG area with interior tBLG and BLG regions. (e) Surface potential image corresponding to (d). (f) Histogram of the surface potentials in (e), indicating a potential difference of ~13 mV between tBLG and BLG. (g and h) Surface potential images of different BLG areas. (i) Plot of the surface potential difference between tBLG and BLG *versus* the twist angle (θ) of tBLG. The shaded circles show clusters of the experimental data and the red dashed lines are for visual guidance. The scale bar represents 6 μm in all the images.

strength of the interlayer electronic coupling in tBLG decreased rapidly. The twist induced the separation of the Dirac cones in two layers. When θ was increased to >20°, the layers were decoupled, and the electronic characteristics could not be distinguished from those of SLG, indicating that for tBLG ($\theta \approx 30°$), the interlayer coupling was negligible.[58] Interlayer electron coupling affects the Fermi energy level, which is reflected by a change in the surface potential. tBLG ($\theta \approx 30°$) can be considered as decoupled bilayer (SLG + SLG) graphene. The surface potential of tBLG ($\theta \approx 30°$) was only slightly higher than that of SLG.

The effects of thermal annealing on the CVD-grown BLG films were investigated *via in situ* KPFM measurements after a sequential annealing process under an H_2/Ar atmosphere, as shown in Fig. 5. Before annealing, the surface potential of tBLG was lower than that of BLG obtained in a previous study, and using the optical image, different regions in the image could be quickly distinguished. Here, we used the KPFM image rather than the Raman spectra to intuitively represent the changes because KPFM has a higher resolution and is more convenient. The surface potential images of a typical tBLG region after annealing at 150, 250, and 350 °C for 2 h and natural cooling to room temperature are shown in Fig. 5(a)–(d). The wrinkles in BLG gradually became smaller and then completely disappeared, which was attributed to the reduction in the interlayer spacing and consequent enhanced interlayer coupling. As shown in the figures, the KPFM contrast of BLG after annealing exhibited no obvious changes; thus, its surface potential change was negligible, which is consistent with its thermal stability. The surface potential of tBLG was almost constant before annealing at 250 °C but was slightly increased after annealing at 350 °C and nearly reached the surface potential value of BLG. This indicated that the twist angle of tBLG was reduced by interfacial sliding due to

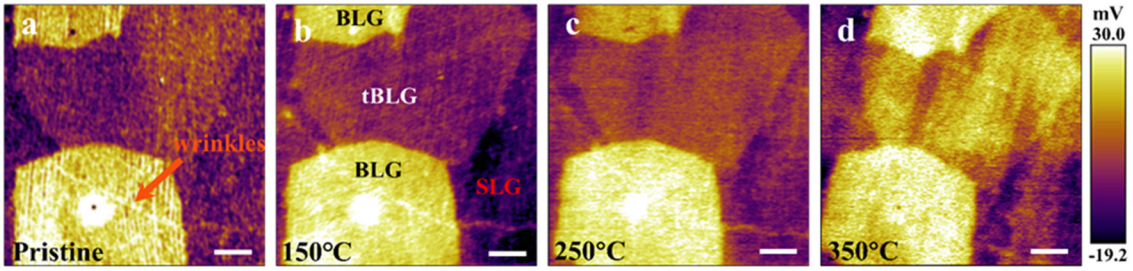

Fig. 5 Effects of thermal annealing on tBLG. (a) KPFM image of a typical tBLG region that has not been annealed. (c and d) Surface potential images of the same regions were obtained by annealing KPFM under an H_2/Ar atmosphere at 150, 250, and 350 °C. The annealing temperatures are shown in the corresponding images. The scale bar represents 6 μm.

the large thermal energy during the annealing process. It appears that the thermal stability of tBLG depends on the grain size.[59,60]

ABA-TLG (Bernal-stacked), ABC-TLG (rhombohedral-stacked), and tTLG were also resolved in the KPFM and Raman measurements. In the future, KPFM investigations of tTLG and the emergent exotic quantum states within the semi-metallic ABA-TLG and semiconducting ABC-TLG can be considered. We attempted to obtain the Moiré pattern image of tBLG using other functional AFM methods. However, surface contamination introduced during the transfer process and the rough surface of the SiO_2/Si substrate degraded our results. A clean transfer method and atomically flat h-BN are needed to prepare appropriate tBLG samples for visualising their Moiré patterns. The in-plane homojunctions of BLG–tBLG can have novel transport properties, which warrant extensive exploration.

Conclusions

We systematically studied the twist angle-dependent surface potential properties of CVD-grown tBLG using KPFM in combination with Raman spectroscopy. First of all, KPFM is used to directly distinguish Bernal-stacked graphene, measure the relationship between the surface potential and the number of layers, and draw the conclusion that the work function decreases with the increase in graphene layer thickness. Then, KPFM is used to directly distinguish the different stacking structures of BLG and tBLG. The relationship between the twist angle and the surface potential in tBLG was established by KPFM imaging and Raman spectroscopy. Different degrees of twist angles were resolved by different contrasts and work function differences. In addition, the thermal stability of twisted bilayer graphene was also studied. However, there are still some unsolved problems. For example, during the CVD growth process, there are four relatively concentrated torsion angle ranges, which may be related to the potential growth mode of the sample, but require further experimental and theoretical demonstrations. The effect of sample transfer or different growth conditions on the relationship between the work function and the number of layers is also investigated. In a word, our research gives another possibility of the work function relationship between the different layers of CVD-grown graphene and also explores the twist angle-related surface potential of tBLG, which lays the foundation for further research on the singular properties of the twisted graphene system.

Materials and methods

Synthesis of CVD multilayer graphene on copper foil

The multilayer graphene film was grown on copper foil *via* low-pressure CVD, as previously reported.[15] During the growth, 2 sccm methane (CH_4) and 30 sccm hydrogen (H_2) were introduced to the chamber at 1030 °C for 40–90 min. After the growth, the chamber was cooled naturally to room temperature in H_2 (30 sccm). The as-grown graphene samples were transferred onto SiO_2/Si using the standard PMMA transfer technique.[40,41] First, graphene was spin-coated onto copper with a thin layer of PMMA. Next, the PMMA/graphene/Cu foil block was soaked in ammonium persulfate for 2 h to etch the copper foil. The PMMA/graphene block was then rinsed with deionised water and transferred onto an SiO_2/Si substrate. Residual PMMA was removed using acetone and isopropyl alcohol. Finally, the graphene/SiO_2/Si samples were thermally annealed under an H_2/Ar atmosphere at 150 °C for 2 h.

Raman and SEM measurements

A WITec 300R confocal Raman system was used for Raman spectroscopy and mapping. The excitation laser was tuned to wavelengths of 532 and 633 nm and the laser power was maintained below 1–2 mW to avoid laser-induced sample heating or damage. WITec Project software (version 5.0) was used for data analysis, creating a histogram of the integrated intensity, and Raman mapping. The topography of BLG transferred onto SiO_2/Si was examined *via* SEM (Hitachi SU-5000) at a voltage of 20 kV.

AFM and KPFM measurements

AFM and KPFM measurements were performed using an Asylum Cypher S atomic force microscope (Oxford Instruments, Asylum Research, Santa Barbara, CA, USA). The

AFM probe was a commercial electrostatic PPP-EFM probe (Nano sensors) with a resonance frequency of ~75 kHz. The KPFM measurements were performed in the dual-pass mode. During the second-pass scanning, the lift height was 20–30 nm. In the KPFM measurements, we used an alternating-current voltage of approximately 2.7–3.2 V. All the AFM measurements were conducted under ambient conditions (a temperature of 23–28 °C and a relative humidity of 20%–30%).

Conflicts of interest

The authors declare that they have no other competing interest.

Acknowledgements

This project was supported by the National Natural Science Foundation of China (NSFC) (No. 61674045), the Ministry of Science and Technology (MOST) of the People's Republic of China (No. 2016YFA0200700), and the Strategic Priority Research Program and the Key Research Program of Frontier Sciences (Chinese Academy of Sciences, CAS) (No. XDB30000000 and QYZDB-SSW-SYS031). Z. H. C. and S. C. were supported by the Fundamental Research Funds for the Central Universities and the Research Funds of Renmin University of China (No. 21XNLG27 and 21XNLG26).

References

1 Y. Cao, V. Fatemi, S. Fang, K. Watanabe, T. Taniguchi, E. Kaxiras and P. Jarillo-Herrero, *Nature*, 2018, **556**, 43–50.
2 M. Yankowitz, S. Chen, H. Polshyn, Y. Zhang, K. Watanabe, T. Taniguchi, D. Graf, A. F. Young and C. R. Dean, *Science*, 2019, **363**, 1059–1064.
3 X. Liu, Z. Wang, K. Watanabe, T. Taniguchi, O. Vafek and J. I. A. Li, *Science*, 2021, **371**, 1261–1265.
4 Y. Choi, H. Kim, Y. Peng, A. Thomson, C. Lewandowski, R. Polski, Y. Zhang, H. S. Arora, K. Watanabe, T. Taniguchi, J. Alicea and S. Nadj-Perge, *Nature*, 2021, **589**, 536–541.
5 A. L. Sharpe, E. J. Fox, A. W. Barnard, J. Finney, K. Watanabe, T. Taniguchi, M. A. Kastner and D. Goldhaber-Gordon, *Science*, 2019, **365**, 605–608.
6 Y. Cao, V. Fatemi, A. Demir, S. Fang, S. L. Tomarken, J. Y. Luo, J. D. Sanchez-Yamagishi, K. Watanabe, T. Taniguchi, E. Kaxiras, R. C. Ashoori and P. Jarillo-Herrero, *Nature*, 2018, **556**, 80–84.
7 X. Lu, P. Stepanov, W. Yang, M. Xie, M. A. Aamir, I. Das, C. Urgell, K. Watanabe, T. Taniguchi, G. Zhang, A. Bachtold, A. H. MacDonald and D. K. Efetov, *Nature*, 2019, **574**, 653–657.
8 G. Lee, R. C. Cooper, S. J. An, S. Lee, A. v. d. Zande, N. Petrone, A. G. Hammerberg, C. Lee, B. Crawford, W. Oliver, J. W. Kysar and J. Hone, *Science*, 2013, **340**, 1073–1076.
9 S. Xing, W. Wu, Y. Wang, J. Bao and S. Pei, *Chem. Chem. Phys.*, 2013, **580**, 62–66.
10 H. Li, H. Ying, X. Chen, D. L. Nika, A. I. Cocemasov, W. Cai, A. A. Balandin and S. Chen, *Nanoscale*, 2014, **6**, 13402–13408.
11 Z. Yu, A. Song, L. Sun, Y. Li, L. Gao, H. Peng, T. Ma, Z. Liu and J. Luo, *Small*, 2020, **16**, 1902844.
12 C. M. Chu and W. Y. Woon, *Nanotechnology*, 2020, **31**, 435603.
13 L. Sun, Z. Wang, Y. Wang, L. Zhao, Y. Li, B. Chen, S. Huang, S. Zhang, W. Wang, D. Pei, H. Fang, S. Zhong, H. Liu, J. Zhang, L. Tong, Y. Chen, Z. Li, M. H. Rümmeli, K. S. Novoselov, H. Peng, L. Lin and Z. Liu, *Nat. Commun.*, 2021, **12**, 2391.
14 C. C. Lu, Y. C. Lin, Z. Liu, C. H. Yeh, K. Suenaga and P. W. Chiu, *ACS Nano*, 2013, **7**, 2587–2594.
15 S. Han, X. Nie, S. Gu, W. Liu, L. Chen, H. Ying, L. Wang, Z. Cheng, L. Zhao and S. Chen, *Appl. Phys. Lett.*, 2021, **118**, 193104.
16 H. Yoo, R. Engelke, S. Carr, S. Fang, K. Zhang, P. Cazeaux, S. H. Sung, R. Hovden, A. W. Tsen, T. Taniguchi, K. Watanabe, G. C. Yi, M. Kim, M. Luskin, E. B. Tadmor, E. Kaxiras and P. Kim, *Nat. Mater.*, 2019, **18**, 448–453.
17 L. Brown, R. Hovden, P. Huang, M. Wojcik, D. A. Muller and J. Park, *Nano Lett.*, 2012, **12**, 1609–1615.
18 A. C. Gadelha, D. A. A. Ohlberg, C. Rabelo, E. G. S. Neto, T. L. Vasconcelos, J. L. Campos, J. S. Lemos, V. Ornelas, D. Miranda, R. Nadas, F. C. Santana, K. Watanabe, T. Taniguchi, B. v. Troeye, M. Lamparski, V. Meunier, V. H. Nguyen, D. Paszko, J. C. Charlier, L. C. Campos, L. G. Cançado, G. Medeiros-Ribeiro and A. Jorio, *Nature*, 2021, **590**, 405–409.
19 Y. Chen, L. Meng, W. Zhao, Z. Liang, X. Wu, H. Nan, Z. Wu, S. Huang, L. Sun, J. Wang and Z. Ni, *Phys. Chem. Chem. Phys.*, 2014, **16**, 21682–21687.
20 T. Benschop, T. A. D. Jong, P. Stepanov, X. Lu, V. Stalman, S. J. v. d. Molen, D. K. Efetov and M. P. Allan, *Phys. Rev. Res.*, 2021, **3**, 013153.
21 D. Wong, K. P. Nuckolls, M. Oh, B. Lian, Y. Xie, S. Jeon, K. Watanabe, T. Taniguchi, B. A. Bernevig and A. Yazdani, *Nature*, 2020, **582**, 198–202.
22 H. Li, R. Papadakis, T. Hussain, A. Karton and J. Liu, *Nano Res.*, 2020, **13**, 1060–1064.
23 X. Huang, L. Chen, S. Tang, C. Jiang, C. Chen, H. Wang, Z. X. Shen, H. Wang and Y. T. Cui, *Nano Lett.*, 2021, **21**, 4292–4298.
24 L. J. McGilly, A. Kerelsky, N. R. Finney, K. Shapovalov, E. M. Shih, A. Ghiotto, Y. Zeng, S. L. Moore, W. Wu, Y. Bai, K. Watanabe, T. Taniguchi, M. Stengel, L. Zhou, J. Hone, X. Zhu, D. N. Basov, C. Dean, C. E. Dreyer and A. N. Pasupathy, *Nat. Nanotechnol.*, 2020, **15**, 580–584.
25 J. Yu, R. Giridharagopal, Y. Li, K. Xie, J. Li, T. Cao, X. Xu and D. S. Ginger, *Nano Lett.*, 2021, **21**, 3280–3286.
26 Y. Luo, R. Engelke, M. Mattheakis, M. Tamagnone, S. Carr, K. Watanabe, T. Taniguchi, E. Kaxiras, P. Kim and W. L. Wilson, *Nat. Commun.*, 2020, **11**, 4209.

27 R. W. Havener, H. Zhuang, L. Brown, R. G. Hennig and J. Park, *Nano Lett.*, 2012, **12**, 3162–3167.
28 A. Niilisk, T. Kahro, V. Kiisk, M. Rähn, H. Alles, J. Aarik and V. Sammelselg, *Open Phys.*, 2015, **13**, 34–40.
29 P. Ramnani, M. R. Neupane, S. Ge, A. A. Balandin, R. K. Lake and A. Mulchandani, *Carbon*, 2017, **123**, 302–306.
30 K. Kim, S. Coh, L. Z. Tan, W. Regan, J. M. Yuk, E. Chatterjee, M. F. Crommie, M. L. Cohen, S. G. Louie and A. Zettl, *Phys. Rev. Lett.*, 2012, **108**, 246103.
31 S. Coh, L. Z. Tan, S. G. Louie and M. L. Cohen, *Phys. Rev. B: Condens. Matter Mater. Phys.*, 2013, **88**, 165431.
32 S. Zhang, A. Song, L. Chen, C. Jiang, C. Chen, L. Gao, Y. Hou, L. Liu, T. Ma, H. Wang, X. Q. Feng and Q. Li, *Sci. Adv.*, 2020, **6**, eabc5555.
33 S. Hussain, R. Xu, S. Ye, L. Lei, X. Liu, R. Xu, L. Xie and Z. Cheng, *Front. Phys.*, 2019, **14**, 33401.
34 S. Hussain, R. Xu, K. Xu, L. Lei, S. Xing, J. Guo, H. Dong, A. Liaqat, R. Iqbal, M. A. Iqbal, S. Gu, F. Cao, Y. J. Li, Y. Sugawara, F. Pang, W. Ji, L. Xie, S. Chen and Z. Z. Cheng, *Front. Phys.*, 2021, **16**, 53504.
35 Y. Yu, Y. Zhao, S. Ryu, L. E. Brus, K. S. Kim and P. Kim, *Nano Lett.*, 2009, **10**, 3430–3434.
36 O. Leenaerts, B. Partoens, F. M. Peeters, A. Volodin and C. V. Haesendonck, *J. Phys.: Condens. Matter*, 2017, **29**, 035003.
37 V. Panchal, R. Pearce, R. Yakimova, A. Tzalenchuk and O. Kazakova, *Sci. Rep.*, 2013, **3**, 2597.
38 D. Ziegler, P. Gava, J. Güttinger, F. Molitor, L. Wirtz, M. Lazzeri, A. M. Saitta, A. Stemmer, F. Mauri and C. Stampfer, *Phys. Rev. B: Condens. Matter Mater. Phys.*, 2011, **83**, 235434.
39 J. T. Robinson, J. Culbertson, M. Berg and T. Ohta, *Sci. Rep.*, 2018, **8**, 2006.
40 H. Ying, W. Wang, W. Liu, L. Wang and S. Chen, *Carbon*, 2019, **146**, 549–556.
41 H. Zhao, X. Xing, G. Zhang, W. Liu, H. Dong, Z. Lu, T. Li, J. Zhang, Z. Cheng, L. Wang and S. Chen, *2D Mater.*, 2022, **9**, 015036.
42 S. Hussain, R. Xu, K. Xu, L. Lei, L. Meng, Z. Zheng, S. Xing, J. Guo, H. Dong, A. Liaqat, M. A. Iqbal, Y. J. Li, Y. Sugawara, F. Pang, W. Ji, L. Xie and Z. Cheng, *Appl. Phys. Lett.*, 2020, **117**, 153102.
43 R. Xu, F. Pang, Y. Pan, Y. Lun, L. Meng, Z. Zheng, K. Xu, L. Lei, S. Hussain, Y. Li, Y. Sugawara, J. Hong, W. Ji and Z. Cheng, *ACS Nano*, 2020, **14**, 13834–13840.
44 L. Lei, Y. Lun, F. Cao, L. Meng, S. Xing, J. Guo, H. Dong, S. Gu, K. Xu, S. Hussain, Y. J. Li, Y. Sugawara, F. Pang, W. Ji, J. Hong, R. Xu and Z. Cheng, *Nanotechnology*, 2021, **32**, 465703.
45 T. Filleter, K. V. Emtsev, T. Seyller and R. Bennewitz, *Appl. Phys. Lett.*, 2008, **93**, 133117.
46 T. Yoon, Q. Wu, D. J. Yun, S. H. Kim and Y. J. Song, *Sci. Rep.*, 2020, **10**, 9870.
47 T. H. Tran, R. D. Rodriguez, M. Salerno, A. Matković, C. Teichert and E. Sheremet, *Carbon*, 2021, **1776**, 431–439.
48 T. C. Barbosa, A. C. Gadelha, D. A. A. Ohlberg, K. Watanabe, T. Taniguchi, G. Medeiros-Ribeiro, A. Jorio and L. C. Campos, *2D Mater.*, 2022, **9**, 025007.
49 S. Pezzini, V. Mišeikis, G. Piccinini, S. Forti, S. Pace, R. Engelke, F. Rossella, K. Watanabe, T. Taniguchi, P. Kim and C. Coletti, *Nano Lett.*, 2020, **5**, 3313–3319.
50 W. Yao, E. Wang, C. Bao, Y. Zhang, K. Zhang, K. Bao, C. K. Chan, C. Chen, J. Avila, M. C. Asensio, J. Zhu and S. Zhou, *Proc. Natl. Acad. Sci. U. S. A.*, 2018, **115**, 6928–6933.
51 B. Deng, B. Wang, N. Li, R. Li, Y. Wang, J. Tang, Q. Fu, Z. Tian, P. Gao, J. Xue and H. Peng, *ACS Nano*, 2020, **14**, 1656–1664.
52 R. He, T. F. Chung, C. Delaney, C. Keiser, L. A. Jauregui, P. M. Shand, C. C. Chancey, Y. Wang, J. Bao and Y. P. Chen, *Nano Lett.*, 2013, **13**, 3594–3601.
53 Y. Hou, X. Ren, J. Fan, G. Wang, Z. Dai, C. Jin, W. Wang, Y. Zhu, S. Zhang, L. Liu and Z. Zhang, *ACS Appl. Mater. Interfaces*, 2020, **12**, 40958–40967.
54 S. Kim, D. Lee, B. Wang, S. J. Yu, K. Watanabe, T. Taniguchi, J. A. Fan, J. Xue and K. Lee, *Appl. Phys. Lett.*, 2021, **118**, 133101.
55 K. D. Park, M. B. Raschke, J. M. Atkin, Y. H. Lee and M. S. Jeong, *Adv. Mater.*, 2017, **29**, 1603601.
56 Y. Chen, L. Meng, W. Zhao, Z. Liang, X. Wu, H. Nan, Z. Wu, S. Huang, L. Sun, J. Wang and Z. Ni, *Phys. Chem. Chem. Phys.*, 2014, **16**, 21682–21687.
57 Y. C. Chen, W. H. Linc, W. S. Tseng, C. C. Chen, G. R. Rossman, C. D. Chen, Y. S. Wu and N. C. Yeh, *Carbon*, 2020, **156**, 212–224.
58 A. Luican, G. Li, A. Reina, J. Kong, R. R. Nair, K. S. Novoselov, A. K. Geim and E. Y. Andrei, *Phys. Rev. Lett.*, 2011, **106**, 126802.
59 J. Kulothungan, M. Muruganathan and H. Mizuta, *Physics*, 2019, **7**, 36.
60 D. Wang, G. Chen, C. Li, M. Cheng, W. Yang, S. Wu, G. Xie, J. Zhang, J. Zhao, X. Lu, P. Chen, G. Wang, J. Meng, J. Tang, R. Yang, C. He, D. Liu, D. Shi, K. Watanabe, T. Taniguchi, J. Feng, Y. Zhang and G. Zhang, *Phys. Rev. Lett.*, 2016, **116**, 126101.